Evolution of lattice defects, disordered/ordered phase transformations and mechanical properties in Ni-Al-Ti intermetallics by high-pressure torsion

Edalati, Kaveh
Department of Materials Science and Engineering, Faculty of Engineering, Kyushu University | WPI, International Institute for Carbon-Neutral Energy Research (WPI-I2CNER), Kyushu University

Daio, Takeshi
Research Laboratory for High Voltage Electron Microscopy, Kyushu University

Horita, Zenji
Department of Materials Science and Engineering, Faculty of Engineering, Kyushu University | WPI, International Institute for Carbon-Neutral Energy Research (WPI-I2CNER), Kyushu University

Kishida, Kyosuke
Department of Materials Science and Engineering, Faculty of Engineering, Kyoto University

他

出版情報：Journal of Alloys and Compounds. 563, pp.221-228, 2013-06-25. Elsevier
バージョン：

Journal of alloys and Compounds 563 (2013) 221–228
Received 16 January 2013; Received in revised from 21 February 2013; Accepted 21 February 2013
Available online 4 March 2013

Evolution of lattice defects, disordered/ordered phase transformations and mechanical properties in Ni-Al-Ti intermetallics by high-pressure torsion

Kaveh Edalati [a,b,*], Takeshi Daio [c], Zenji Horita [a,b], Kyosuke Kishida [d], Haruyuki Inui [d]

[a] Department of Materials Science and Engineering, Faculty of Engineering, Kyushu University, Fukuoka 819-0395, Japan
[b] WPI, International Institute for Carbon-Neutral Energy Research (WPI-I2CNER), Kyushu University, Fukuoka 819-0395, Japan
[c] Research Laboratory for High Voltage Electron Microscopy, Kyushu University, Fukuoka 819-0395, Japan
[d] Department of Materials Science and Engineering, Faculty of Engineering, Kyoto University, Kyoto 606-8501, Japan

Abstract

Powder mixtures of Ni–25 mol.% Al–25 mol.% Ti were subjected to severe plastic deformation using high-pressure torsion (HPT) to examine the formation of ternary ordered intermetallics. In consistency with the Al–Ni and Ti–Al systems, in which the in situ formation of binary ordered intermetallics was achieved during HPT, a partially-ordered nanostructured B2-Ni(Al,Ti) phase with ~11 nm grain size and high dislocation density, $>10^{16}$ m^2, was formed in the Ni–Al–Ti system. The hardness-strain behavior of the Ni–Al–Ti mixture was similar to pure aluminum having a hardness maximum followed by a strain softening at large strains. The B2 phase transformed to a fully-ordered Ni_2AlTi phase with $L2_1$ structure after annealing at 873 K with an activation energy of 270 kJ/mol. Atomic-scale elemental mapping using scanning transmission electron microscopy confirmed the occurrence of ordering after annealing as well as partial twining. Micropillar compression tests showed that both yield stress and plasticity increased after annealing, and high strength and high ductility with values as 3.6 GPa and 7%, respectively, were achieved.

Keywords: Severe plastic deformation (SPD); Nanostructure; Twining; Micropillar compression test; Strain softening; Heusler phases

* Corresponding author at: Department of Materials Science and Engineering, Faculty of Engineering, Kyushu University, Fukuoka 819-0395, Japan. Tel./fax: +81 92 802 2992.
E-mail address: Kaveh.edalati@zaiko6.zaiko.kyushu-u.ac.jp (K. Edalati).

1. Introduction

Among different severe plastic deformation (SPD) methods [1,2], high-pressure torsion (HPT) has capability of continuously imposing extremely large shear strains under high pressures [3,4]. The HPT method is applicable for grain refinement in a wide range of materials such as metallic materials [1-5], semiconductors [1,6], intermetallics [7], amorphous materials [8] and ceramics [9]. In addition to the grain refinement, HPT provides opportunity for several other applications: (i) attainment of ultrahigh strength and high ductility [10], consolidation of metallic powders [11] and machining chips [12], (ii) partial consolidation of hard and brittle materials such as amorphous [13] and ceramic materials [14], (iii) control the phase transformations in several materials such as Ti [15,16], Zr [17,18], Zr-Nb [19], Si [6], TiNi [20], ZrO_2 [9] and supersaturated Al alloys [21], (iv) improvement of multifunctionality [13,22].

A recent application of HPT is for production of nanostructured intermetallics from their elemental constituents at low temperatures [23,24]. The method was applied to powder mixtures of the Al-Ni and Ti-Al systems and it was found that, in addition to powders consolidation and grain refinement, the binary ordered intermetallics with high strength and high ductility were formed by high-strain induced solid-state reactions. Despite these reports, there is limited information about the formation of ternary intermetallics during HPT. It is noted that the synthesis of ternary intermetallics is generally more complicated than the binary intermetallics because of the complex interaction and diffusion of the components. For example, attempts to produce a Ni_2AlTi intermetallic, so-called Heusler alloy, with the $L2_1$ crystal structure may lead to a partially-ordered B2 structure, or a fully-disordered BCC phase or even an amorphous phase [25-27].

In this study, HPT is applied to a Ni-Al-Ti powder mixture to examine whether the ordered Ni_2AlTi intermetallic forms. The evolution of lattice defects, nanostructures and mechanical properties along with HPT processing as well as after subsequent annealing are investigated by X-ray diffraction (XRD) analysis, scanning electron microscopy (SEM), transmission electron microscopy (TEM), atomic-scale scanning transmission microscopy (STEM), differential scanning calorimetry (DSC), hardness measurement and micropillar compression test.

2. Experimental Materials and Methods

Pure Ni (99.99%) powders were mixed with 25 mol.% Al (99.99%) and 25 mol.% Ti (99.9%) powders by mechanical agitation, where the initial morphology of the Ni, Al and Ti powders are shown in Fig. 1. HPT was conducted at 573 K to consolidate the powder mixture to discs with 10mm diameter and 0.8mm thickness under a pressure of P = 6 GPa. Shear strain $\gamma = 2\pi rN/h$ (r: distance from the disc center, N: number of turns, h: thickness of disc), was introduced through rotations for either N = 3, 10, 50 or 120 turns with a rotation speed of 1 rpm. The samples processed for N = 50 were subsequently annealed at 873 K for 1 and 24 h.

The HPT-processed discs were first polished to a mirror-like surface and Vickers microhardness was measured with an applied load of 200 g for 15 s along the radii at 8 different radial directions. Second, XRD analysis was performed using the Cu Kα radiation in a scanning step of 0.01° and a scanning speed of 0.5 °/min. Third, for DSC, the disc samples processed for N =

50 were cut to small pieces at 2-5 mm away from the center. Such pieces with a total mass of ~75 mg were subjected to DSC using heating rates of 2, 3, 5, 10, 15, 20, and 30 K/min. Fourth, for TEM and STEM, thin foils were prepared from the discs at 4 mm away from the disc center with a focused ion beam (FIB) system. TEM and Cs-corrected STEM were performed at 300 and 200 kV, respectively, for microstructure observation, for recording selected-area electron diffraction (SAED) patterns and for atomic-scale energy dispersive X-ray spectrometery (EDS). Fifth, square-shaped micropillars with a side length of ~4 μm and a height of ~12 μm were prepared from the discs at ~4 mm away from the center using focused ion beam (FIB) technique so that the side surfaces of the pillars become perpendicular to the disc surface. Compression test was conducted on the micropillars using a microhardness testing machine equipped with a flat diamond tip with a diameter of 20 μm at a nominal stress rate of 10 MPa/s, which corresponds to an initial strain rate of 10^{-4} s^{-1}. Sixth, the micropillars were observed by SEM under an applied voltage of 15 kV.

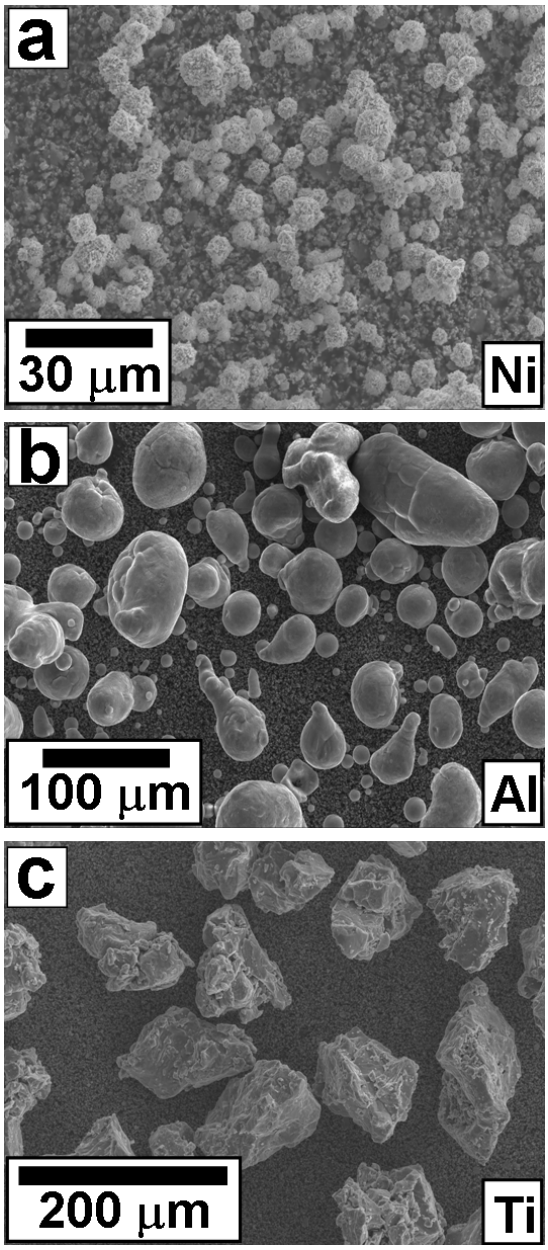

Figure 1. Morphology of (a) Ni, (b) Al and (c) Ti powders observed using SEM.

3. Results and Discussion

3.1. Disordered and ordered phases formation

XRD profiles for the as-received powders, samples after different numbers of turns and samples processed for N = 50 and subjected to subsequent annealing at 873 K for 1 and 24 h are shown in Fig. 2, where (b) is an enlarged view of (a).

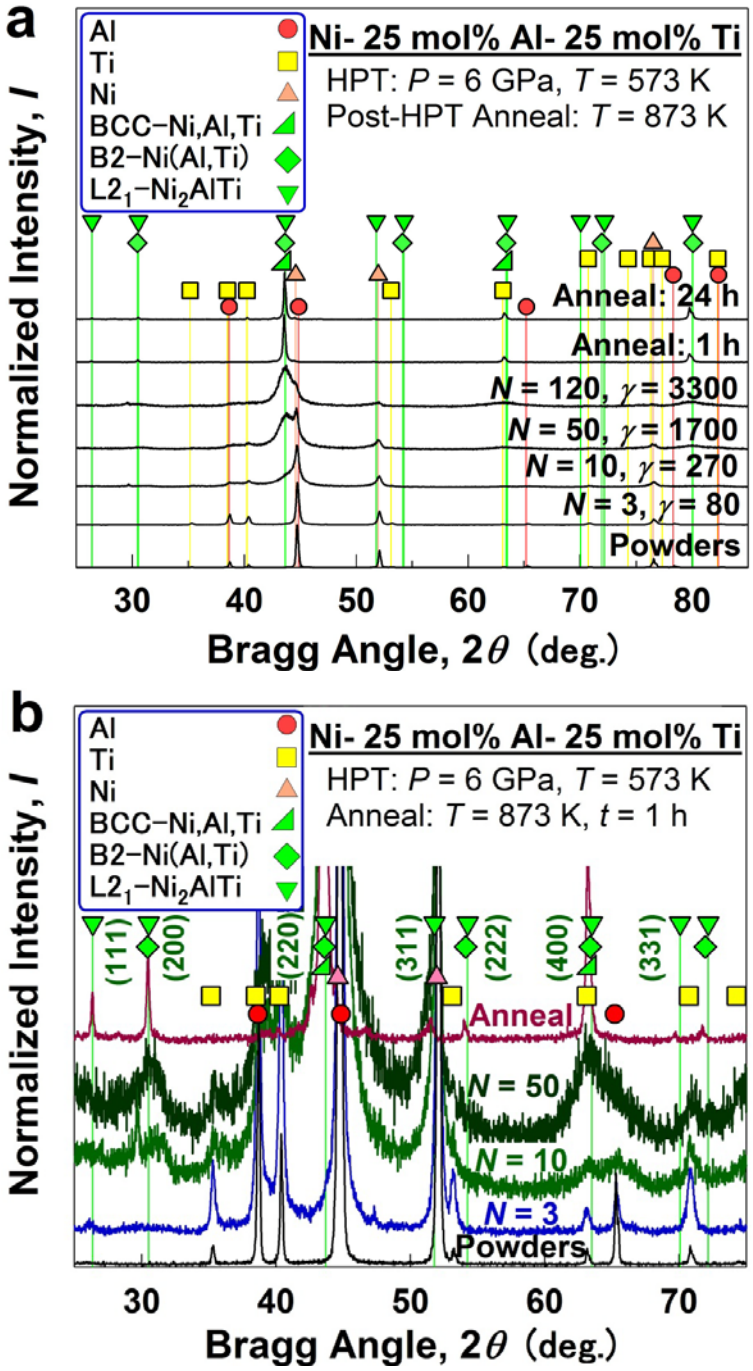

Figure 2. XRD profiles for (a) samples processed by HPT at 573 K for N = 3, 10, 50 and 120 and samples annealed at 873 K for 1 and 24 h after HPT processing including as-received powder mixtures, and (b) samples processed for N = 50 before and after annealing including as-received powder mixtures in enlarged scale to check formation of ordered B2-Ni(Al,Ti) and $L2_1$-Ni_2AlTi phases.

No phase transformation could be detected at the early stages of straining after $\gamma = 80$ or $N = 3$ within the sensitivity limits of the current XRD experiments. Peaks for the partially-ordered B2-Ni(Al,Ti) phase with a lattice parameter of $a = 0.293$ nm appears after $\gamma = 270$ or $N = 10$. It should be noted that most peaks for the fully-disordered BCC-Ni,Al,Ti, the partially-ordered B2-Ni(Al,Ti) phase and the fully-ordered $L2_1$ phases superimpose, but the B2 phases has a superlattice peak at $2\theta = 30.5^o$ and the $L2_1$ phases has two superlattice peaks at $2\theta = 26.4^o$ and $2\theta = 30.5^o$ which can be used for their recognition. A comparison between the peak for the elemental constituents at $2\theta = 44.6\text{-}44.8^o$ and the peak for the B2-Ni(Al,Ti) phase at $2\theta = 43.7^o$ indicates that the fraction of the B2-Ni(Al,Ti) phase increases with increasing the shear strain. After $N = 3$, there is just one peak at $2\theta = 44.6\text{-}44.8^o$, indicating that no B2 phases is formed. The peak is extended to the lower angles after $N = 10$, indicating that small amounts of B2 phase are formed. After $N = 50$, a peak at $2\theta = 43.7^o$ is visible, showing that large amounts of B2 phase are formed. The material at large shear strains (e.g. $\gamma = 3300$ or $N = 120$) after HPT processing consists mainly of the B2 phase, although some fractions of unreacted elemental constituents (Ni, Al and Ti) are still present even after HPT for $N = 120$. Appearance of the (111) peak at $2\theta = 26.4^o$ after the post-HPT annealing confirms that the material transforms to the fully-ordered $L2_1$-Ni_2AlTi phase with a lattice parameter of $a = 0.584$ nm. Therefore, in consistency with the Al-Ni and Ti-Al systems, in which the formation of ordered phases occurs during HPT processing [23,24], a partially-ordered B2 phase is formed in the Ni-Al-Ti system during HPT processing and the partially-ordered B2 phase transformed to a fully-ordered $L2_1$ phase by subsequent annealing.

It should be noted that Ti exhibits a pressure-induced phase transformation from an α phase with the *hcp* crystal structure to an ω phase with the simple hexagonal structure during HPT under the pressures higher than 4 GPa at room temperature [15,16]. The HPT was conducted under 6 GPa in this work, but XRD analysis confirmed that the transformation to ω phase was not detected after various numbers of turns. The difference arises because the processing temperature of 573 K used in this study is high enough to induce the reverse phase transformation to α phase (the temperature for revere phase transformation is ~423 K [16]).

3.2. Activation energy for ordering

The variation of heat flow with temperature after DSC analysis of the sample processed by HPT for $N = 50$ is shown in Fig. 3(a) and (b) at different heating rates, where (a) is an enlarged view of (a) to check the peak temperatures. A peak corresponding to the formation of the ordered $L2_1$-Ni_2AlTi phase [26] appears at a temperature in the range of 750-850 K for each of the heating rates on the HPT-processed sample. Examination of Fig. 3(a) shows two points. First, the area surrounded by each peak in W/g increases with increasing the heating rate. This increase is a consequence of the fact that the area surrounded by each peak in J/g is dependent on the transformation enthalpy and independent of the heating rate. However, the time for heat generation decreases with increasing the heating rate, and thus, the heating power (area surrounded by each peak in W/g) should increase in proportion to the heating rate. Second, the peak temperature shifts

to higher temperatures by increasing the heating rate. The peak shifts can be used to evaluate the activation energies using the Kissinger equation [28] as described in details in Ref. [29]

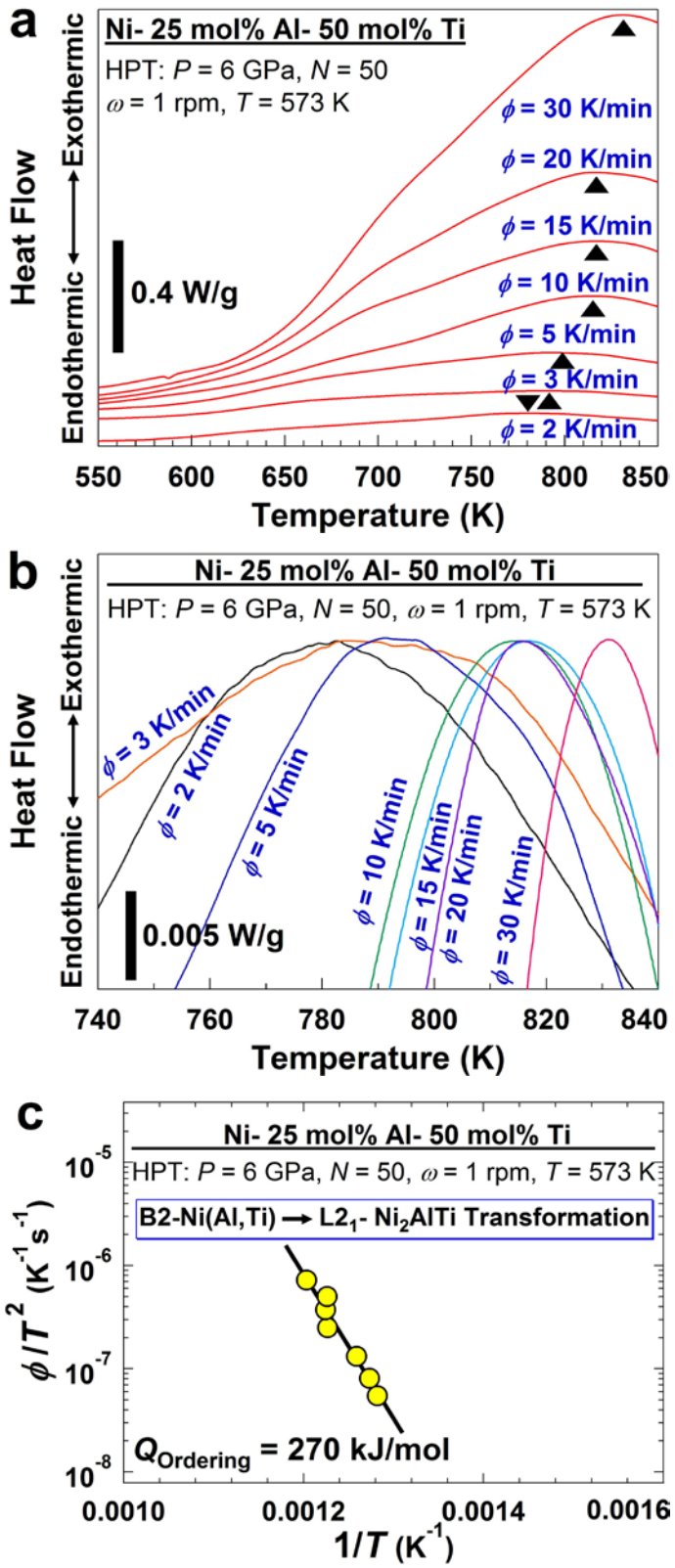

Figure 3. (a) DSC curves obtained using different heating rates, (b) enlarged scale of (a) to show peak temperatures, and (c) ϕ/T^2 plotted against $1/T$ (T: peak temperatures, ϕ: heating rate) for sample processed by HPT at 573 K for N = 50. Slopes in (b) represent activation energy for formation of $L2_1$-Ni_2AlTi phase.

$$\frac{\phi}{T^2} = A\exp(\frac{-Q}{kT}) \quad (1)$$

where ϕ is the heating rate, T is the peak temperature, Q is the activation energy and k is Boltzmann constant. Figure 3(c) plots ϕ/T^2 against $1/T$ in the semi-logarithmic scale, showing that all data points are well on a single straight line. Thus, the slope of the line gives rise to Q = 270 kJ/mol for ordering and formation of the $L2_1$-Ni_2AlTi phase from B2-Ni(Al,Ti). Such a high activation energy for the ordering may explain why the fully-ordered $L2_1$ phase could not be formed during the HPT processing at 573 K. Stability of disordered or partially-ordered phases during HPT which was reported in several other intermetallic systems [20,30] can be another reason for the formation of B2 phase rather than $L2_1$ phase.

3.3. High dislocation density

Figure 2 shows that a significant peak broadening occurs by the HPT processing but disappears after the subsequent annealing at 873 K. This indicates unambiguously that recovery and recrystallization occurs during the annealing. If the lattice strain and crystallite size are calculated from the peak broadening using the Williamson-Hall method and the dislocation density is calculated as $\rho = 14.4\varepsilon^2/b^2$ (ε: lattice strain, b: burgers vector) [31], it turns out that the dislocation density and crystallite size are $5\text{x}10^{16}$ m^{-2} and 5 nm, respectively, in the B2-Ni(Al,Ti) phase after the HPT processing and $3\text{x}10^{14}$ m^{-2} and 51 nm in the $L2_1$-Ni_2AlTi phase after the subsequent annealing. It should be noted that the scattering of data points from the Williamson-Hall equation was appreciable in this study. The dislocation density after HPT processing in this study is comparable to those reported for HPT-processed pure metals [29,32], alloys [33,34] and ceramics [9]. However, the crystallite size of 5 nm is considerably smaller than those reported in HPT-processed pure metals and alloys [32].

3.4. Nanostructure formation

Microstructures are shown in Figs. 4, where TEM images including SAED patterns are shown in (a) and (b) for the samples processed by HPT for N = 50, and in (c-f) for the same sample after post-HPT annealing at 873 K for 24 h. In Fig. 4, micrographs (b) and (d) are dark-field images of (a) and (c), respectively, which were taken with diffracted beams indicated by arrows in the SAED patterns. TEM characterization indicates several important points. First, the microstructures consist of nanograins after HPT processing. Second, the grain size increases after subsequent annealing. Third, ring patterns from the SAED analyses indicate that most of the nanograins are separated by high angles of misorientations after HPT and the misorientation angles remain high even after the annealing. Fourth, being similar to the Ti-Al system, the severely-deformed samples exhibit nanotwin formation by subsequent annealing because of the low stacking fault energy [24]. Fifth, microstructure is heterogeneous after annealing which includes nanotwinned grains as marked **A** in (c), nanograins as marked **B** in (e) and submicrometer grains as marked **C** in (f).

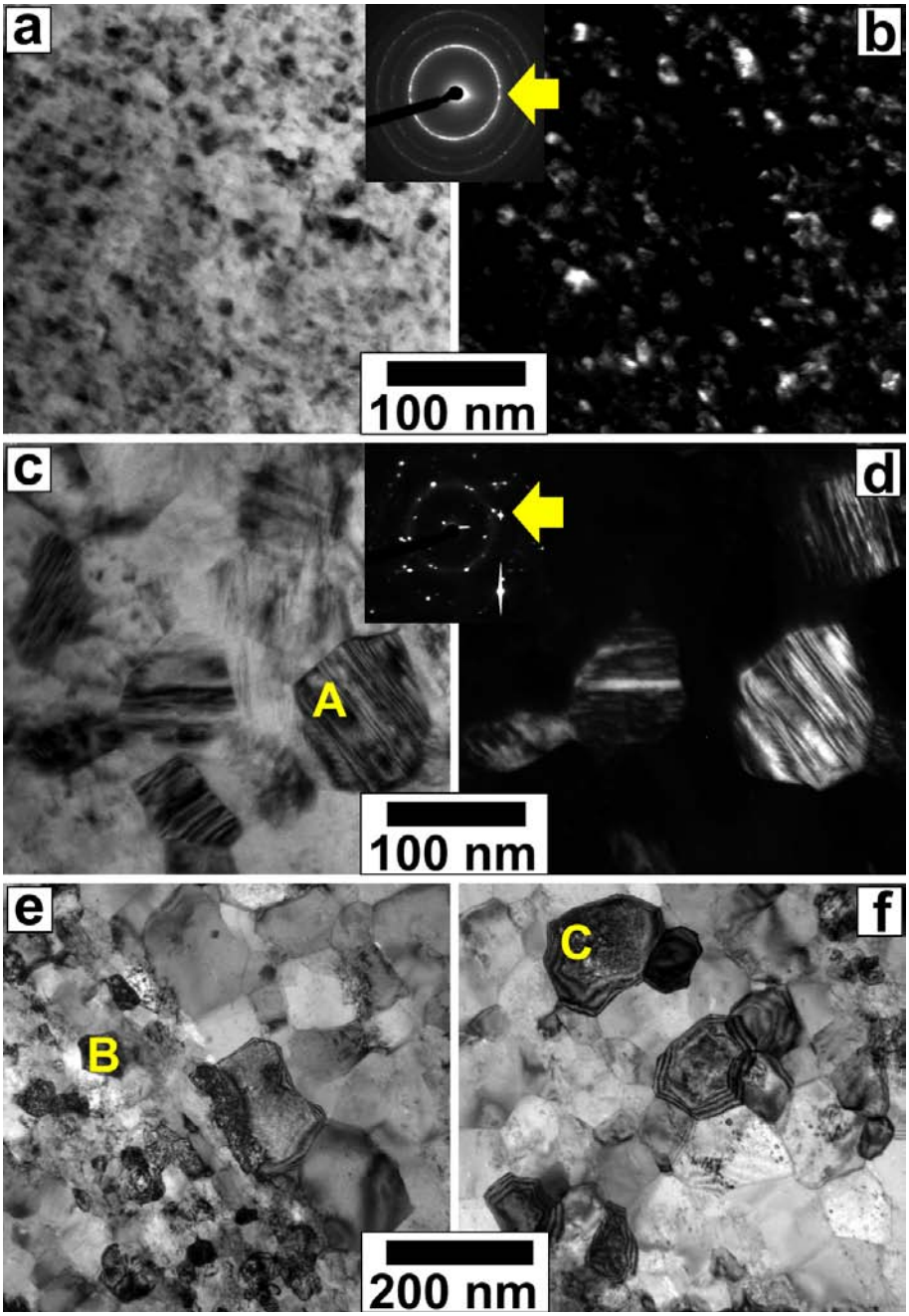

Figure 4. TEM micrographs and SAED patterns of (a, b) samples processed by HPT at 573 K for N = 50 and (c-f) same sample annealed at 873 K for 24 h, where micrographs (b) and (d) are dark-field images of (a) and (c), respectively. Dark-field images were taken with diffracted beams indicated by arrows in SAED patterns.

The grain size distribution at the steady state after HPT processing for N = 50 and after post-HPT annealing at 873 K for 24 h is shown in Fig. 5. The grain sizes were obtained from the dark-field images as shown in Figs. 4(b) and (d) by measuring the two orthogonal axes of the bright areas corresponding to more than 100 grains. The average grain size after HPT is ~11 nm and is well in the nanometer range. The grain size increases by annealing but the average grain size still remains small as ~170 nm. The grain size of 11 nm is significantly smaller than the values reported

for HPT-processed pure metals and alloys [3,4], but it is comparable to or even smaller than the grain sizes of HPT-processed intermetallics [7], semiconductors [1,6] and ceramics [9].

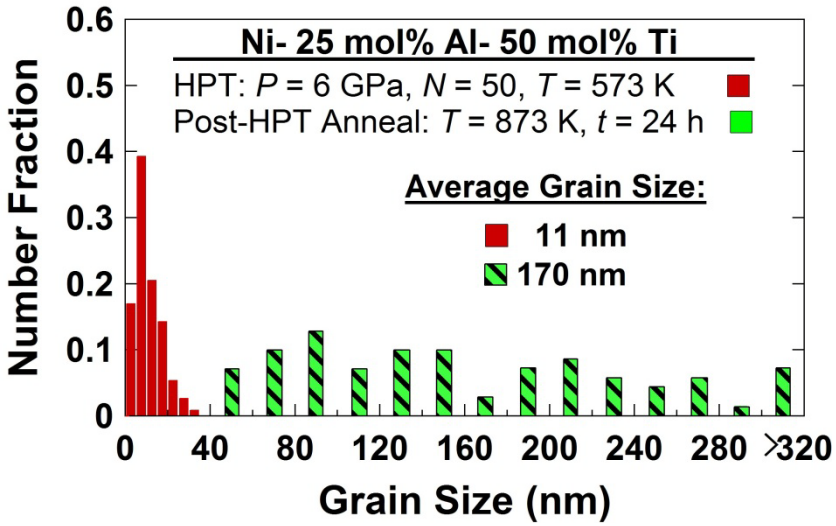

Figure 5. Number fraction of grain size distribution for sample processed by HPT at 573 K for N = 50 and sample annealed at 873 K for 24 h after HPT processing.

Figure 6 shows high-resolution (a-d) TEM and (e,f) STEM images including the corresponding diffractograms obtained by Fast Fourier Transform (FFT) analyses: (a-c) a sample processed by HPT for N = 50 and (d-f) the same sample after post-HPT annealing at 873 K for 24 h. Note that (b) and (c) are lattice images of the grains marked **a** and **b** in (a) obtained by inverse FFT. Examination of Fig. 6 indicates several important points.

(i) It is confirmed that the nanograins form after HPT processing and they coarsen after annealing.

(ii) An inspection of (f) indicates that the partially-ordered phase formed after HPT processing transforms to an ordered $L2_1$-Ni_2AlTi phase in consistency with the XRD analyses. The formation of the ordered phase was confirmed by atomic-scale EDS as will be discussed below in Fig. 7.

(iii) Nanotwins with an average width of ~5 nm as in (e) are formed by post-HPT annealing.

(iv) The grain boundaries after HPT are ill-defined and their width is even higher than 1 nm in (a) which is consistent with Ref. [35], but the grain boundaries become sharper after the post-HPT annealing in (d). It should be noted that this ill-defined nature is not due to the inclination of the boundaries with respect to the surface normal because well-defined condition was not attained even after tilting the sample during the TEM observations. If the width of grain boundaries is considered to be 1 nm, estimation shows that 15 vol.% of the sample is occupied by grain boundaries for the grain size of 11 nm after the HPT processing, but less than 1 vol.% of the sample with the grain size of ~170 nm after the post-HPT annealing.

(v) Figures. 6(b) and (c) clearly show that there is an edge dislocation in the interior of grains. If the dislocation density is estimated as $\rho = n/(\pi d^2/4)$ (n: average number of dislocations in

one grain, *d*: average grain size) an estimation results in ρ = ~10^{16} m^{-2}, provided that a single edge dislocation exists in one grain with the grain size of 11 nm. As compared in Table 1, this value is reasonably consistent with the value of 5x10^{16} m^{-2} calculated using XRD analyses.

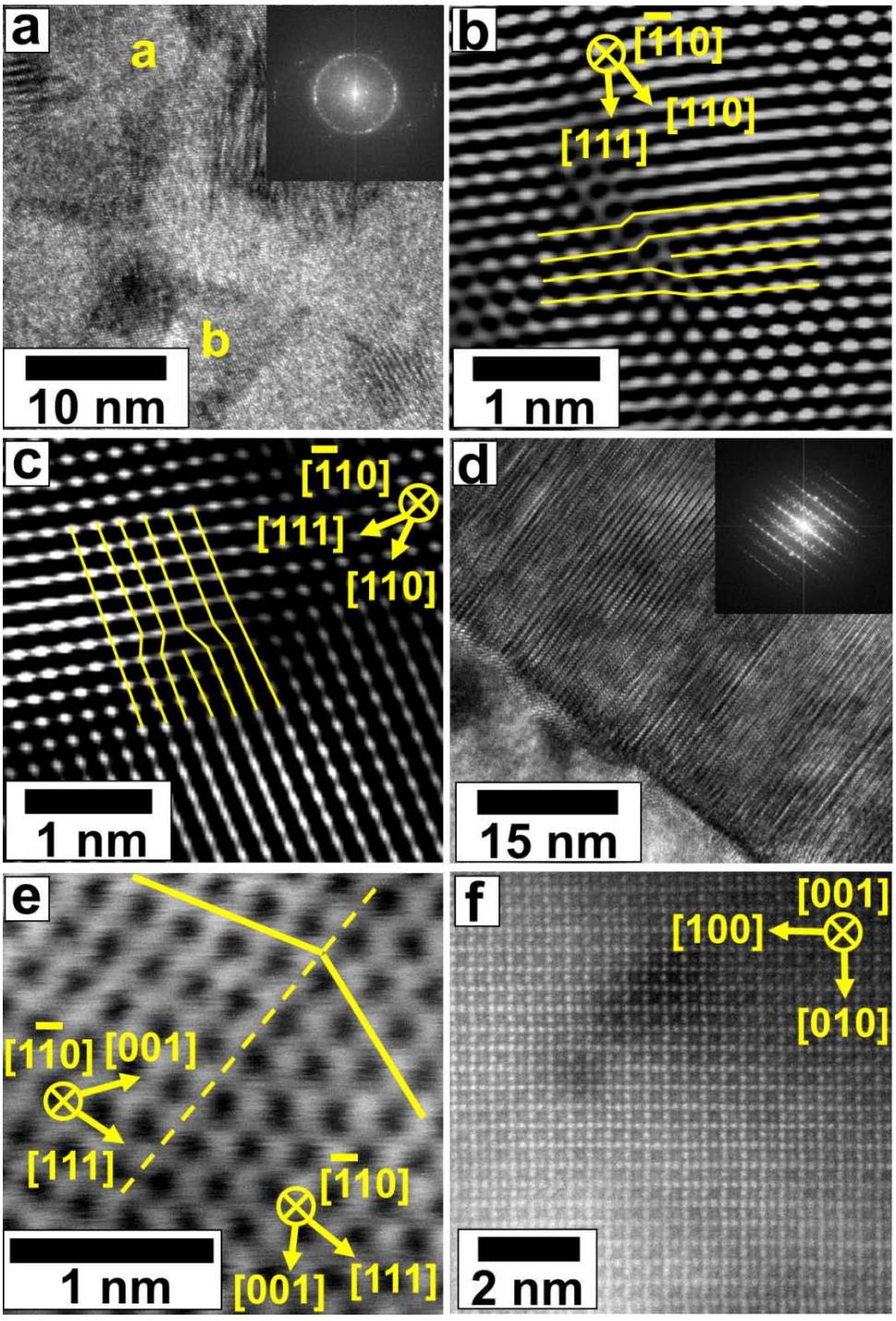

Figure 6. (a) TEM High resolution image and corresponding FFT analysis for sample processed by HPT at 573 K for *N* = 50, (b, c) lattice images of edge dislocations obtained by inverse Fast Furrier Transform from grains marked **b** and **c** in (a), respectively, (d) TEM high resolution image and corresponding FFT analysis for sample annealed at 873 K for 24 h after HPT processing, (e, f) STEM lattice images of twin and $L2_1$-Ni_2AlTi ordered phase, respectively, for sample annealed at 873 K for 24 h after HPT processing.

Table 1. Grain size, volume fraction of grain boundaries, dislocation density and twin width for sample processed by HPT at 573 K for N = 50 and same sample after annealing at 873 K for 24 h, measured by TEM and XRD analyses.

	Grain Size (nm)		**Grain Boundary (vol.%)**	**Dislocation Density (m^{-2})**	**Twin Width (nm)**
Method	TEM	XRD	TEM	XRD	TEM
As-HPT	11	5	15	$5X10^{16}$	---
Anneal	170	51	1	$3X10^{14}$	5

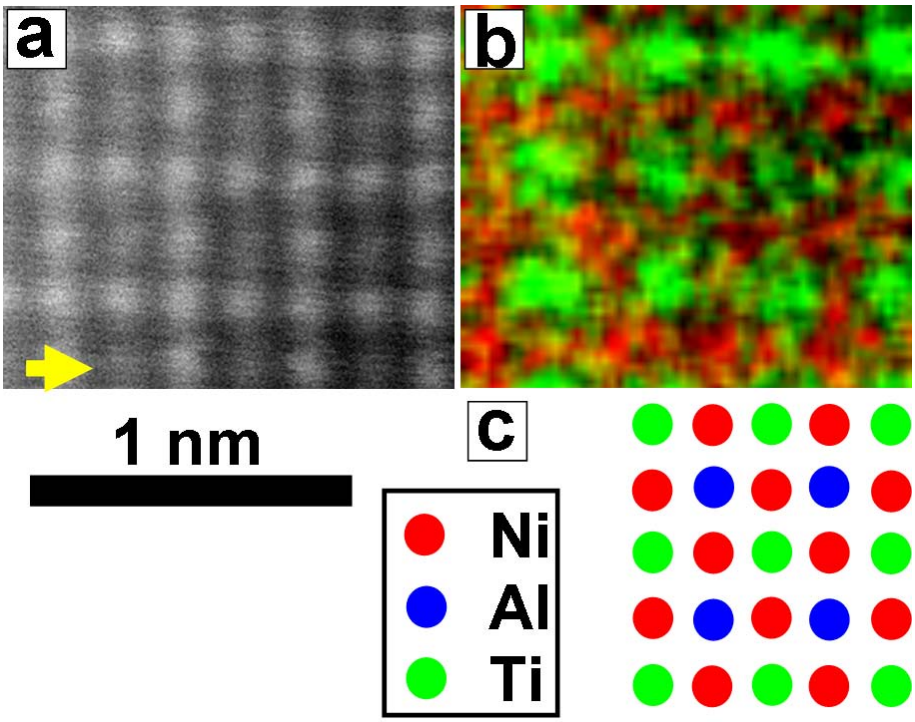

Figure 7. (a) STEM-HAADF lattice image and (b) corresponding atomic-scale EDS mappings with Ni (red color) and Ti (green color) including (c) simulated arrangement of Ni, Al and Ti atoms for samples processed by HPT at 573 K for N = 50 and annealed at 873 k for 1 and 24 h after HPT processing.

Figures 7 shows (a) a STEM high-angle annular dark-field (HAADF) lattice image and (b) the corresponding atomic-scale EDS mapping of Ni (red), Al (blue) and Ti (green) including (c) the simulated arrangement of Ni, Al and Ti atoms for the sample processed by HPT at 573 K for N = 50 and post-HPT annealed at 873 k for 24 h. It should be noted that the intensity of EDS mapping of Al was too low to be recorded. Since the atomic number of Al is smaller than those of Ni and Ti, the dim points as indicated by the arrow in the HAADF lattice image in (a) should correspond to Al. It is apparent from Fig. 7(a-c) that Ni, Al and Ti are present in a regular atomic arrangement which is well consistent with the $L2_1$ ordered structure.

3.5. Hardness-strain behavior

Figure 8(a) shows the hardness variation with the distance from the center of disc after HPT processing for N = 3, 10, 50 and 120. The hardness increases with an increasing number of turns and an increasing distance from the disc center. The saturation of the hardness level appears in the discs after 10 or more turns and in particular the hardness values after 50 and 120 turns lie close to this saturated level. To demonstrate the hardness behavior with respect to shear strain, all hardness values in Fig. 8(a) are plotted against the shear strain in Fig. 8(b). It is apparent that hardness increases with increasing the shear strain, reaches a maximum at an equivalent strain of ~300, decreases to a constant level at an equivalent strain of ~500, and remains at this constant level with increasing the strain.

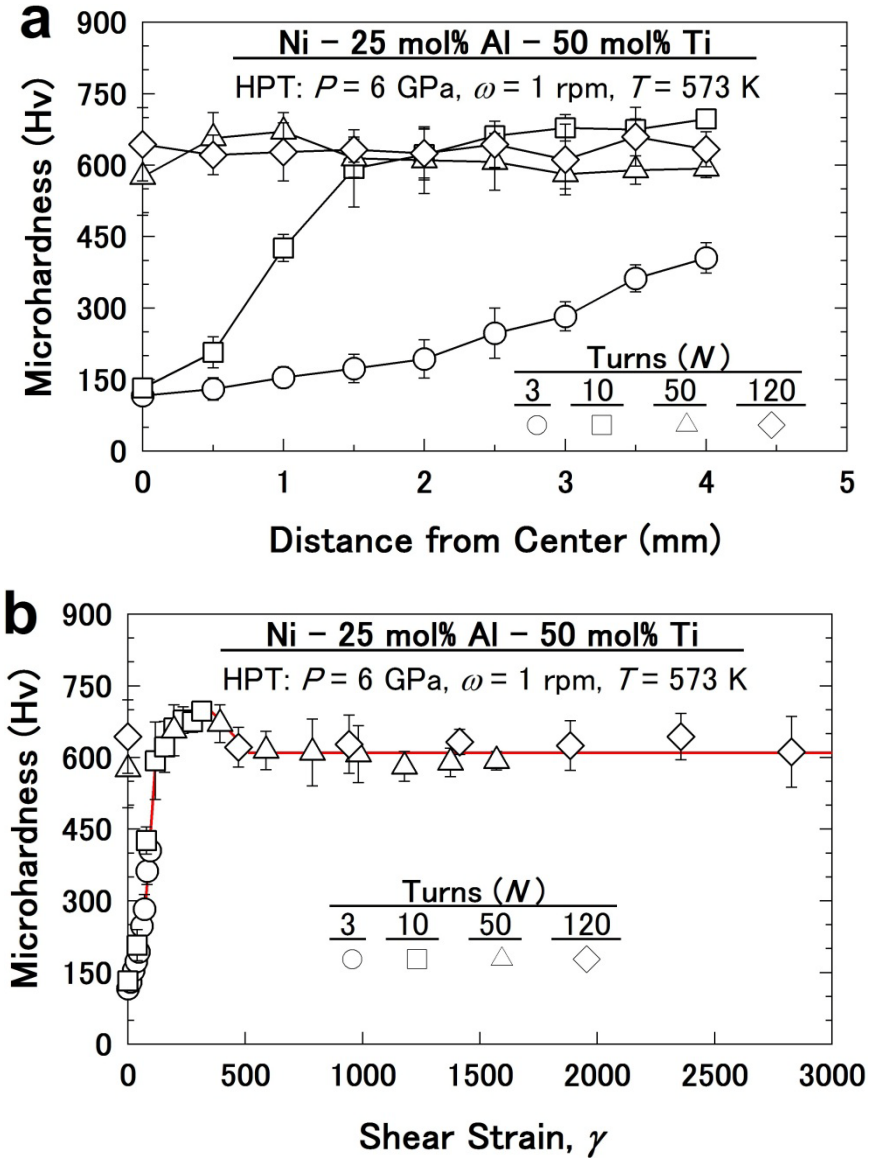

Figure 8. Vickers microhardness plotted against (a) distance from disc center and (b) shear strain for samples processed by HPT at 573 K for N = 3, 10, 50 and 120.

This unusual hardness-strain behavior is basically similar to the earlier observation of pure metals with low melting temperatures such as Al [36-39], Mg [40] and Zn [41,42]. This behavior can be also detected in other alloys and metals when processed at high homologous temperatures [41,43-45]. The softening of pure metals at large strains was attributed to easy recovery of dislocation and easy recrystallization [36,46]. However, the softening at large strains in the Ni-Al-Ti system cannot be attributed to the dislocation recovery or recrystallization because the dislocation density is quite high and the grain size is very small at the steady state. One reason for the softening at large strains may be due to the reverse Hall-Petch effect. Although the Hall-Petch effect suggests that the yield strength increases with the inverse square root of the grain size, recent investigations documented that a softening occurs as the grain size is reduced below ~25 nm because of the grain boundary-associated mechanisms such as grain boundary diffusion and sliding [47]. The high dislocation density may be another reason for the softening at the steady state. Hardness increases with increasing the dislocation density in coarse-grained materials; however, Huang *et al.* [48] found that the effect of dislocations on the hardness can be totally different in nanometals. They reported a hardening by annealing and a softening by plastic deformation in SPD-processed nanometals. They suggested that, because there are no dislocations within nanograins after annealing, extra stress is required to create dislocations for deformation. However, since some dislocations are present after SPD, the sample deforms readily as there is no requirement for the generation of mobile dislocation.

3.6. Hardening by annealing

The hardness values were measured after annealing of the HPT-processed samples and plotted in Fig. 9 together with those at the saturation for the as-HPT-processed samples including those for pure Al, Ti and Ni after HPT processing at 298 K for comparison. The hardness values in this study are much higher than the saturation levels for pure Al, Ti and Ni reported in Ref. [16,41]. Despite the relatively high annealing temperature as 873 K, the HPT-processed samples exhibit abrupt increases in the hardness after the annealing. Here, the amounts of these increases range up to ~250 Hv, although the hardness decreases slightly with increasing the annealing time for 24 h.

The main reason for the hardness increase by the annealing must be due to completion of solid-state reactions and formation of a fully-ordered $L2_1$-Ni_2AlTi phase. Formation of a large fraction of twin boundaries [24], the reverse Hall-Petch effect [47] and the paradox of dislocations disappearance [48] may also partly contribute to the hardening by annealing in this study.

3.7. Ultrahigh strength and high plasticity

Two representative stress-strain curves before and after annealing the HPT-processed samples are delineated in Fig. 10 from micropillar compression tests conducted at room temperature with a pillar size of ~4x4x12 μm^3, as attempted in earlier papers [24,49,50]. The sample after HPT but before annealing, which consists mainly of a B2 phase, exhibits a high yield strength, ~1.6 GPa and high ultimate strength, ~2 GPa, with an appreciable plasticity as 4%. The sample after subsequent annealing, which contains the $L2_1$ phase, exhibits a high plasticity as ~7%, an enhanced

yield strength of ~3.3 GPa and an ultrahigh ultimate strength of ~3.6 GPa.

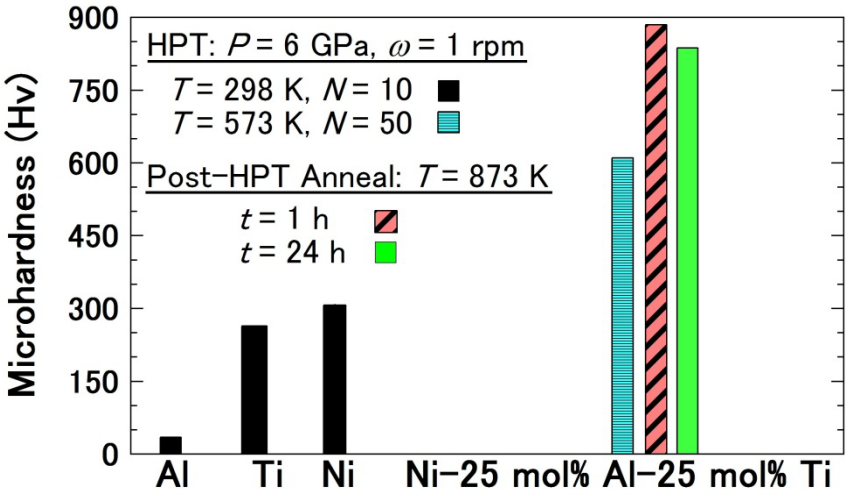

Figure 9. Steady-state hardness levels for samples processed by HPT at 573 K for N = 50 and annealed at 873 k for 1 and 24 h after HPT processing including steady-state hardness levels for Al, Ti and Ni processed by HPT at 298 K taken from Ref. [16,41].

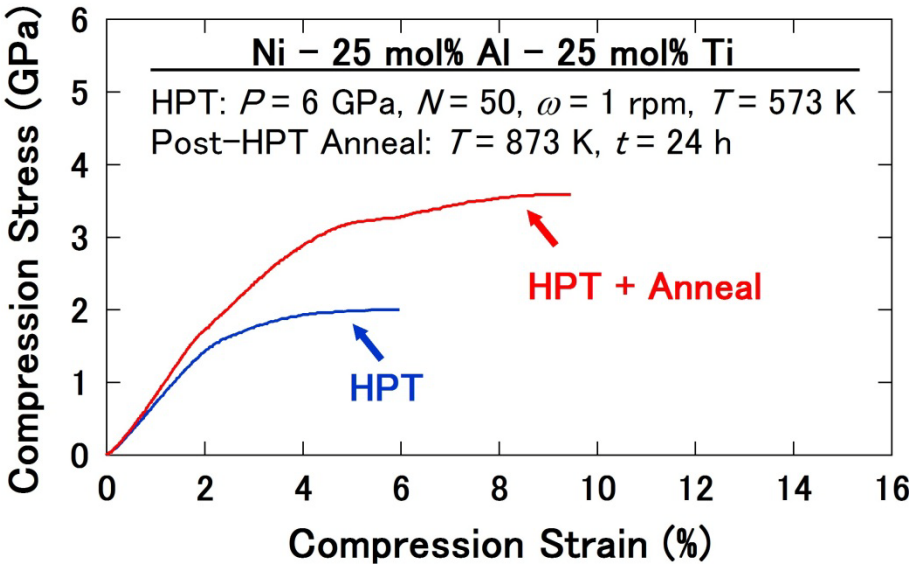

Figure 10. Nominal stress versus nominal strain curves for samples processed by HPT at 573 K for N = 50 and annealed at 873 k for 24 h after HPT processing obtained by micropillar compression tests.

Figs. 11 and 12 show micropillars of the HPT-processed samples before and after the annealing, respectively, where (a), (b) and (c) are before compression tests, after compression test and magnified views including the fractured parts. An additional micrograph is shown in Fig. 12(d) for a close observation of the deformed surface. Inspection of the pillars after the compression

reveals that the pillar prior to the annealing is failed with cleavage-like fracture with no significant localized plasticity but the pillar after the annealing exhibits many plastically deformed areas. The plasticity of 7% in the $L2_1$-Ni_2AlTi phase is considered as a high plasticity level for intermetallic materials. Although the pillars with small sizes exhibit artificially high plasticity [51], the pillar size of 4 μm is large enough to eliminate the size effect on the plasticity [24]. The high strength obtained after annealing should be mainly due to the formation of ordered phases. However, the main mechanism underlying the high plasticity in the $L2_1$-Ni_2AlTi phase is not well understood yet. The high plasticity may be due to three main reasons: first, presence of nanotwins before deformation [52] as shown in Figs. 3(b,c), second, activation of different deformation mechanisms such as dislocation slip, as shown in Fig. 12(d), twining and grain boundary sliding during the deformation [10,24] and third, heterogeneous grain size distribution [53,54], as shown in Figs. 4 and 5.

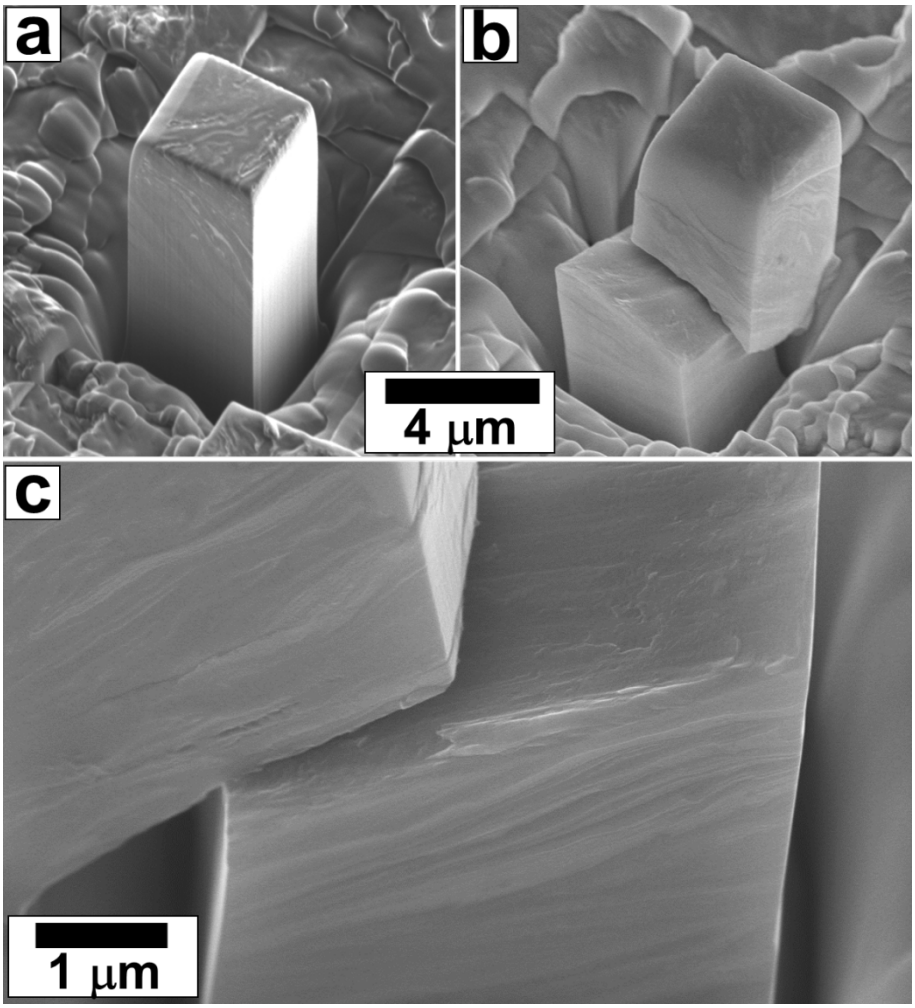

Figure 11. Appearance of pillar for sample processed by HPT at 573 K for N = 50. (a) before compression observed by secondary electrons in FIB and (b, c) after compression observed by secondary electrons in SEM, where (c) is magnified view of (b).

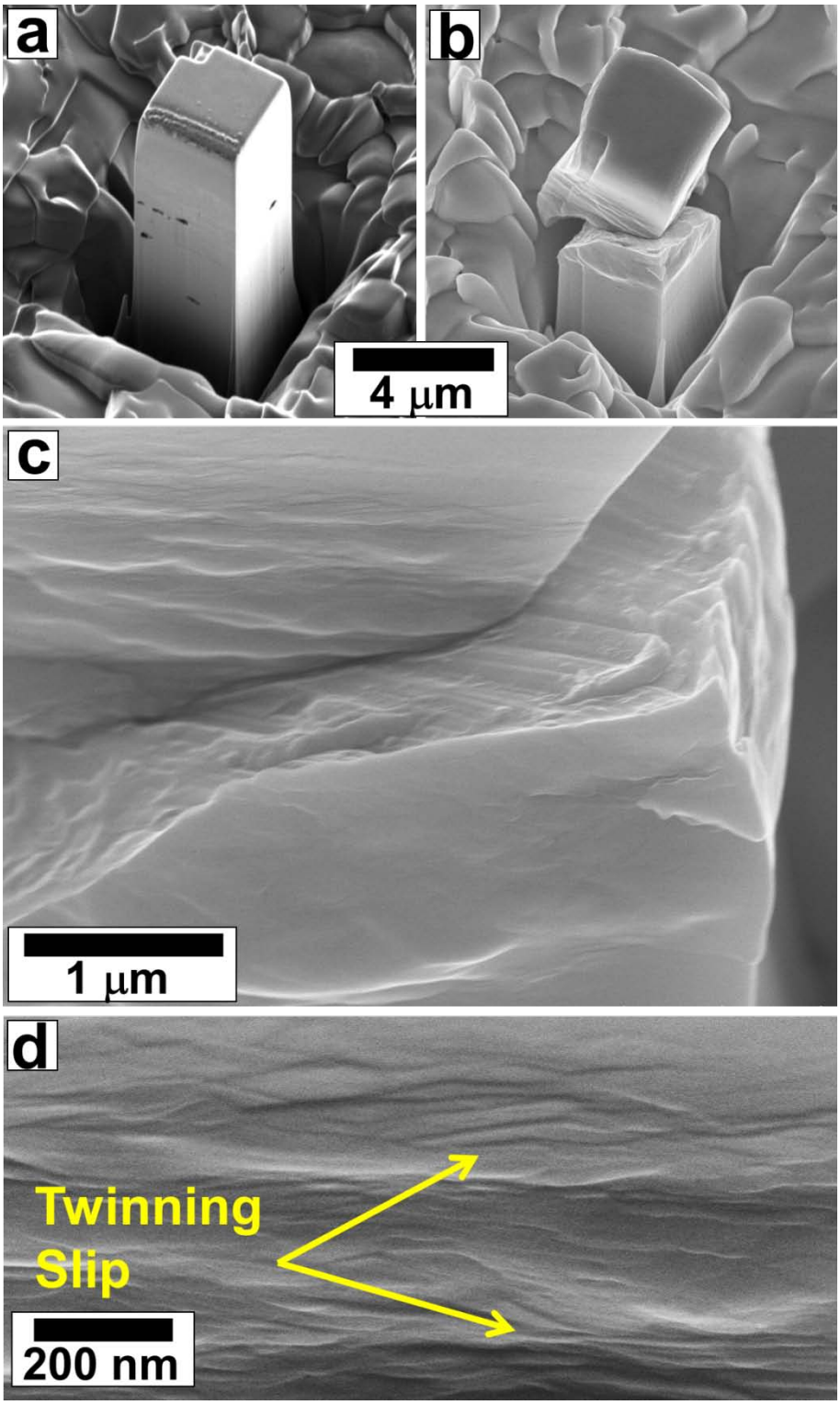

Figure 12. Appearance of pillar for sample processed by HPT and successively annealed at 873 k for 24 h (a) before compression observed by secondary electrons in FIB and (b-d) after compression observed by secondary electrons in SEM, where (c) and (d) are magnified views of (b).

4. Conclusions

Powder mixtures of Ni- 25 mol.% Al- 25 mol.% Ti were subjected to HPT processing at 573

K and successively to annealing at 873 K. The following conclusions were drawn from this study.

1. A partially-ordered B2-Ni(Al,Ti) phase with an average grain size of ~11 nm containing a high dislocation density as high as $>10^{16}$ m^2 was produced in situ during processing by HPT.
2. The hardness-strain behavior was similar to metals with low melting temperatures, having a hardness maximum followed by a softening to a steady state.
3. The B2 phase transformed to fully-ordered $L2_1$-Ni_2AlTi phase with an average grain size of ~170 nm after annealing with an activation energy for ordering of 270 kJ/mol.
4. Nanotwins with an average twin width of ~5 nm were partially formed after annealing the HPT-processed samples.
5. The material exhibited a hardening by annealing because of the formation of the $L2_1$-Ni_2AlTi intermetallic. Micropillar compression tests showed that the material had a high strength of ~3.6 GPa and a high plasticity of ~7% after the annealing.

Acknowledgements

One of the authors (KE) thanks the Japan Society for Promotion of Science (JSPS) for a postdoctoral scholarship. This work was supported in part by the Light Metals Educational Foundation of Japan, in part by a Grant-in-Aid for Scientific Research from the MEXT, Japan, in Innovative Areas "Bulk Nanostructured Metals", in part by Kyushu University Interdisciplinary Programs in Education and Projects in Research Development (P&P), in part by Grant-in-Aid for Scientific Research (A) (no. 24246113) from the MEXT, Japan, and in part by the Advanced Low Carbon Technology Research and Development Program of the Japan Science and Technology Agency (JST).

References

[1] R.Z. Valiev, R.K. Islamgaliev, I.V. Alexandrov, Prog. Mater. Sci. 45 (2000) 103-189.

[2] R.Z. Valiev, Y. Estrin, Z. Horita, T.G. Langdon, M.J. Zehetbauer, Y.T. Zhu, JOM 58 (4) (2006) 33-39.

[3] A.P. Zhilyaev, T.G. Langdon, Prog. Mater. Sci. 53 (2008) 893-979.

[4] R. Pippan, S. Scheriau, A. Taylor, M. Hafok, A. Hohenwarter, A. Bachmaier, Annu. Rev. Mater. Res. 40 (2010) 319-343.

[5] J. Wongsa-Ngam, M. Kawasaki, T.G. Langdon, J. Mater. Sci. 47 (2012) 7782-7788.

[6] Y. Ikoma, K. Hayano, K. Edalati, K. Saito, Q. Guo, Z. Horita, Appl. Phys. Lett. 101 (2012) 121908.

[7] O. Ciuca, K. Tsuchiya, Y. Yokoyama, Y. Todaka, M. Umemoto, Mater. Trans. 51 (2010) 14-22.

[8] A.R. Yavari, W.J. Botta, C.A.D. Rodrigues, C. Cardoso, R.Z. Valiev, Scripta Mater. 46 (2002) 711-716.

[9] K. Edalati, S. Toh, Y. Ikoma, Z. Horita, Scripta Mater. 65 (2011) 974-977.

[10] R.Z. Valiev, I.V. Alexandrov, Y.T. Zhu, T.C. Lowe, J. Mater. Res. 17 (2002) 5-8.

[11] Z. Lee, F. Zhou, R.Z. Valiev, E.J. Lavernia, S.R. Nutt, Scripta Mater. 51 (2004) 209-214.

[12] A.P. Zhilyaev, A.A. Gimazov, G.I. Raab, T.G. Langdon, Mater. Sci. Eng. A 486 (2008) 123-128.
[13] A. Revesz, A. Kis-Toth, L.K. Varoa, E. Schafler, I. Bakonvi, T. Spassov, Int. J. Hydrogen Energy 37 (2012) 5769-5776.
[14] K. Edalati, Z. Horita, Scripta Mater. 63 (2010) 174-177.
[15] Y. Todaka, J. Sasaki, T. Moto, M. Umemoto, Scripta Mater. 59 (2008) 615-618.
[16] K. Edalati, E. Matsubara, Z. Horita, Metall. Mater. Trans. A, 40 (2009) 2079-2086.
[17] A.P. Zhilyaev, I. Sabirov, G. Gonzales-Doncel, J. Molina-Aldarequia, B. Srinivasarao, M.T. Perez-Prado, Mater. Sci. Eng. A 528 (2011) 3496-3505.
[18] M.T. Perez-Prado, A.A. Gimazov, O.A. Ruano, M.E. Kassner, A.P. Zhilyaev, Scripta Mater. 58 (2008) 219-222.
[19] B.B. Straumal, A.S. Gornakova, A.A. Mazilkin, O.B. Fabrichnaya, M.J. Kriegel, B. Baretzky, J.Z. Jiang, S.V. Dobatkin, Mater. Lett. 81 (2012) 225-228.
[20] J.Y. Huang, Y.T. Zhu, X.Z. Liao, R.Z. Valiev, Phil. Mag. Lett. 84 (2004) 183-190.
[21] B.B. Straumal, B. Baretzky, A.A. Mazilkin, F. Phillipp, O.A. Kogtenkova, M.N. Volkov, R.Z. Valiev, Acta Mater. 52 (2004) 4469-4478.
[22] M. Zehetbauer, R. Grossinger, H. Krenn, M. Krystian, R. Pippan, P. Rogl, T. Waitz, R. Wurschum, Adv. Eng. Mater. 12 (2010) 692-700.
[23] K. Edalati, S. Toh, M. Watanabe, Z. Horita, Scripta Mater. 66 (2012) 386-389.
[24] K. Edalati, S. Toh, H. Iwaoka, M. Watanabe, Z. Horita, D. Kashioka, K. Kishida, H. Inui, Scripta Mater. 67 (2012) 814-817.
[25] W.J. Boettinger, L.A. Bendersky, J.A. West, M.J. Aziz, Mater. Sci. Eng. A 133 (1991) 592-595.
[26] Z.G. Liu, J.T. Guo, Z.Q. Hu, J. Alloys Compd. 234 (1996) 106-110.
[27] H.H. Sheu, L.C. Hsiung, J.R. Sheu, J. Alloys Compd. 469 (2009) 483-487.
[28] H.E. Kissinger, Anal. Chem. 29 (1957) 1702-1706.
[29] D. Setman, E. Schafler, E. Korznikova, M.J. Zehetbauer, Mater. Sci. Eng. A. 493 (2008) 116-122.
[30] C. Rentenberger, C. Mangler, S.G. Scheriau, R. Pippan, H.P. Karnthaler, Mater. Sci. Forum 584-586 (2008) 422-427.
[31] G. K. Williamson and R. E. Smallman: Acta Cryst. 7 (1954) 574-581.
[32] J. Cubicza, N.Q. Chinh, T. Csanadi, T.G. Langdon, T. Ungar, Mater. Sci. Eng. A 462 (2007) 86-90.
[33] E.Y. Yoon, D.J. Lee, T.S. Kim, H.J. Chae, P. Jenei, J. Gubicza, T. Ungar, M. Janecek, J. Vratna, S. Lee, H.S. Kim, J. Mater. Sci. 47 (2012) 7117-7123
[34] P. Jeni, J. Gubicza, E.Y. Yoon, H.S. Kim, J. Alloys Compd. 539 (2012) 32-35.
[35] X. Sauvage, G. Wilde, S.V. Divinski, Z. Horita, R.Z. Valiev, Mater. Sci. Eng. A 540 (2012) 1-12.
[36] C. Xu, Z. Horita, T.G. Langdon, Acta Mater. 55 (2007) 203-212.
[37] Y. Harai, Y. Ito, Z. Horita, Scripta Mater. 58 (2008) 469-482.

[38] Y. Ito, Z. Horita, Mater. Sci. Eng. A 503 (2009) 32-36.
[39] M. Kawasaki, R.B. Figueiredo, T.G. Langdon, Acta Mater. 59 (2011) 308-316.
[40] K. Edalati, A. Yamamoto, Z. Horita, T. Ishihara, Scripta Mater. 64 (2011) 880-883.
[41] K. Edalati, Z. Horita, Mater. Sci. Eng. A 528 (2011) 7514-7523.
[42] B. Srinivasarao, A.P. Zhilyaev, T.G. Langdon, M.T. Perez-Prado, Mater. Sci. Eng. A 562 (2013) 196-202.
[43] K. Edalati, Y. Ito, K. Suehiro and Z. Horita, Inter. J. Mater. Res., 100 (2009) 1668-1673.
[44] Y. Huang, R.B. Figueiredo, T. Baudin, F. Brisset, T.G. Langdon, Adv. Eng. Mater. 14 (2012) 1018-1026.
[45] Y. Huang, R.B. Figueiredo, T. Baudin, F. Brisset, T.G. Langdon, J. Mater. Sci. 47 (2012) 7796-7806.
[46] K. Edalati, Z. Horita, T. Furuta, S. Kuramoto, Mater. Sci. Eng. A 559 (2013) 506-509.
[47] M.A. Meyers, A. Mishra, D.J. Benson, Prog. Mater. Sci. 51 (2006) 427-556.
[48] X. Huang, N. Hansen, N. Tsuji, Science, 312 (2006) 249-251.
[49] K. Fujimura, K. Kishida, K. Tanaka, H. Inui, Mater. Res. Soc. Symp. Proc. 1295 (2011) 201-206.
[50] Y.B. Wang, D.D. Que, X.H. Wang, Y. Cao, X.Z. Liao, M. Kawasaki, S.P. Ringer, Z. W. Shan, T.G. Langdon, J. Shen, Acta Mater. 60 (2012) 253-260.
[51] M.D. Uchic, D.M. Dimiduk, J.N. Florando, W.D. Nix, Science 305 (2004) 986-989.
[52] K. Lu, L. Lu, S. Suresh, Science 324 (2009) 349-352.
[53] Y. Wang, M. Chen, F. Zhou, E. Ma, Nature 419 (2002) 912-915.
[54] C.C. Koch, Scripta Mater. 49, 657 (2003) 657-662.